Pyruvate Kinase Regulates the Pentose-Phosphate Pathway in Response to Hypoxia in *Mycobacterium tuberculosis*

Wenhe Zhong[1,2,†], Jingjing Guo[3,4,†], Liang Cui[1,†], Yok Hian Chionh[1,‡], Kuohan Li[2,5,6], Abbas El Sahili[2,6], Qixu Cai[7], Meng Yuan[8,§], Paul A.M. Michels[8], Linda A. Fothergill-Gilmore[8], Malcolm D. Walkinshaw[8], Yuguang Mu[6], Julien Lescar[2,6,] and Peter C. Dedon[1,9,]

1 - Antimicrobial Resistance Interdisciplinary Research Group, *Singapore–MIT Alliance for Research and Technology, 1 CREATE Way, 138602, Singapore*
2 - NTU Institute of Structural Biology, *Nanyang Technological University, 636921, Singapore*
3 - Singapore Centre for Environmental Sciences Engineering (SCELSE), *Nanyang Technological University, 60 Nanyang Drive, 637551, Singapore*
4 - College of Life Sciences, *Nanjing Agricultural University, Nanjing 210095, China*
5 - Lee Kong Chian School of Medicine, *Nanyang Technological University, 59 Nanyang Drive, 636921, Singapore*
6 - School of Biological Sciences, *Nanyang Technological University, 60 Nanyang Drive, 637551, Singapore*
7 - Division of Life Science, *State Key Laboratory of Molecular Neuroscience, Hong Kong University of Science and Technology, Clear Water Bay, Kowloon, Hong Kong, China*
8 - Institute of Quantitative Biology, *Biochemistry and Biotechnology, University of Edinburgh, King's Buildings, Edinburgh EH9 3BF, UK*
9 - Department of Biological Engineering, *Massachusetts Institute of Technology, Cambridge, MA 02139, USA*

Correspondence to Yuguang Mu, Julien Lescar and Peter C. Dedon: *J. Lescar is to be contacted at: NTU Institute of Structural Biology, Nanyang Technological University, 636921, Singapore; P.C. Dedon is to be contacted at: Antimicrobial Resistance Interdisciplinary Research Group, Singapore–MIT Alliance for Research and Technology, 1 CREATE Way, 138602, Singapore. ygmu@ntu.edu.sg, julien@ntu.edu.sg, pcdedon@mit.edu*
https://doi.org/10.1016/j.jmb.2019.07.033

Abstract

In response to the stress of infection, *Mycobacterium tuberculosis* (Mtb) reprograms its metabolism to accommodate nutrient and energetic demands in a changing environment. Pyruvate kinase (PYK) is an essential glycolytic enzyme in the phosphoenolpyruvate–pyruvate–oxaloacetate node that is a central switch point for carbon flux distribution. Here we show that the competitive binding of pentose monophosphate inhibitors or the activator glucose 6-phosphate (G6P) to *Mtb*PYK tightly regulates the metabolic flux. Intriguingly, pentose monophosphates were found to share the same binding site with G6P. The determination of a crystal structure of *Mtb*PYK with bound ribose 5-phosphate (R5P), combined with biochemical analyses and molecular dynamic simulations, revealed that the allosteric inhibitor pentose monophosphate increases PYK structural dynamics, weakens the structural network communication, and impairs substrate binding. G6P, on the other hand, primes and activates the tetramer by decreasing protein flexibility and strengthening allosteric coupling. Therefore, we propose that *Mtb*PYK uses these differences in conformational dynamics to up- and down-regulate enzymic activity. Importantly, metabolome profiling in mycobacteria reveals a significant increase in the levels of pentose monophosphate during hypoxia, which provides insights into how PYK uses dynamics of the tetramer as a competitive allosteric mechanism to retard glycolysis and facilitate metabolic reprogramming toward the pentose-phosphate pathway for achieving redox balance and an anticipatory metabolic response in Mtb.

Introduction

Mycobacterium tuberculosis (Mtb), the etiologic agent of tuberculosis (TB), replicates, evolves, and persists within human hosts by successfully adapting to the environmental challenges imposed by the human immune system [1–4]. Following phagocytosis by macrophages, Mtb mainly relies on lipids as carbon and energy sources. However, co-metabolism and metabolic plasticity of central carbon metabolism (CCM), which includes glycolysis, gluconeogenesis, the pentose-phosphate pathway (PPP), the tricarboxylic acid (TCA) cycle, and the glyoxylate shunt, are also essential in Mtb physiology and pathogenicity and help fine-tune carbon and energy metabolism [5–8]. Recently, Eoh *et al*. [9,10] reported that the adaptation of Mtb to hypoxia was accompanied by the accumulation of glycolytic and PPP intermediates, as an anticipatory metabolic regulatory response required for cell cycle re-entry. Currently, transcriptional, epitranscriptional, and metabolic responses have been extensively characterized to investigate the regulatory adaptation of Mtb to stress [4,7,9,11]. The allosteric regulation of a metabolic enzyme has recently received increasing attention as a key mechanism governing rapid cellular response and adaptation [6,8,12]. Here we describe how the glycolytic enzyme pyruvate kinase (PYK) in Mtb tightly governs the phosphoenolpyruvate (PEP)–pyruvate–oxaloacetate node by a conformational dynamics-driven mechanism that not only activates but also inhibits activity using a single remote allosteric site.

Recently, we showed that glucose 6-phosphate (G6P) allosterically activates *Mtb*PYK and binds at a previously unknown site in the C-domain adjacent to the canonical site for AMP [12] (Fig. S1). This newly discovered allosteric site was designated as the "sugar monophosphate site." However, its additional ability to act as an inhibitory allosteric site remained to be discovered. The only reported effector site that binds allosteric inhibitors of PYK was observed in M2PYK in human cancer cells, where Yuan *et al*. [13] recently revealed that a single amino-acid site in M2PYK provides a competition mechanism to select between activators (serine and histidine) and inhibitors (phenylalanine, alanine, tryptophan, methionine, valine, and proline) acting as a rapid-response nutrient sensor to rebalance cellular metabolism.

Here, we searched for potential modulators of *Mtb*PYK activity by screening a collection of sugar monophosphates (Fig.1). Interestingly, in contrast to the hexose monophosphate G6P, we found three structurally similar pentose monophosphates acted as inhibitors instead of activators of *Mtb*PYK. Furthermore, a crystal structure showed that the pentose monophosphate ribose 5-phosphate (R5P) also binds to the sugar monophosphate site, which suggests that this single effector site provides a switch point selecting between inhibitor and activator to tightly control enzyme activity. Thermal stability

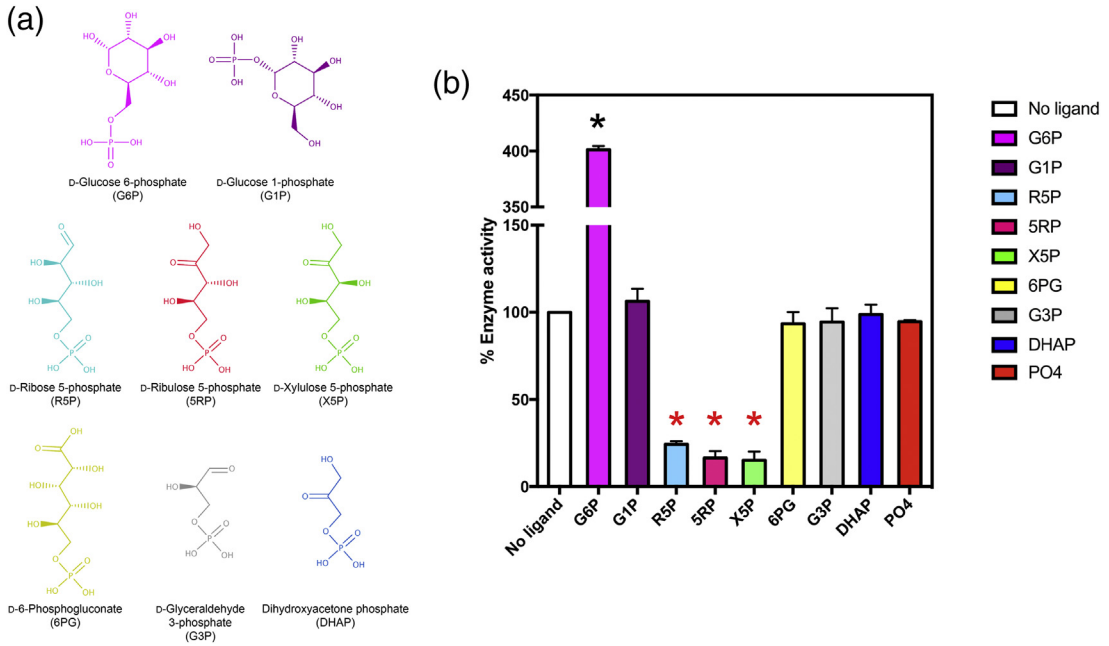

Fig. 1. Pentose phosphate metabolites inhibit enzyme activity of *Mtb*PYK. (a) Structures of sugar monophosphate metabolites selected for activity testing against *Mtb*PYK. (b) The regulation of *Mtb*PYK activity by sugar monophosphates. The black and red asterisks indicate enzyme activation and inhibition, respectively. G6P was tested at 0.2 mM, and other metabolites including PO_4^{3-} were tested at 1.25 mM. All data are mean ± SEM for N = 3.

studies along with structural information indicate that the pentose monophosphate inhibits *Mtb*PYK by destabilizing the active state of the enzyme, while the activator G6P strongly stabilizes the active conformation. This observation is further elaborated by molecular dynamic (MD) simulations showing that *Mtb*PYK provides a conformational dynamics-driven allosteric mechanism for sensing either activator or inhibitor, thereby modifying the MD of the enzyme.

An observed hypoxia-induced metabolic shift toward the PPP in the Mtb surrogate, *Mycobacterium bovis* BCG, is consistent with a pentose monophosphate-dependent inhibition of *Mtb*PYK activity in response to low oxygen. Importantly, Anastasiou *et al*. [14] discovered that, in cancer cells, the inhibition of human M2PYK through cysteine oxidation also enhanced the metabolic flux toward PPP as an antioxidant response. However, unlike human M2PYK, *Mtb*PYK is able to respond to multiple complex sugar monophosphate signals. It thereby provides the bacteria at the critical PEP–pyruvate–oxaloacetate node with a complex and rapid-response allosteric mechanism to facilitate changes required to adapt to challenging environments.

Results

Pentose monophosphates inhibit *Mtb*PYK

We recently discovered a unique sugar monophosphate site on *Mtb*PYK where binding of the hexose phosphate G6P allosterically activated the enzyme [12]. Structurally, the negatively charged phosphate of G6P was locked in place tightly by two salt bridges and three hydrogen bonds. This motivated us to ask if other sugar monophosphate metabolites with structures similar to G6P could be recognized by this effector site and function as enzyme modulators. To test this hypothesis, we first investigated the enzymic effects of a series of sugar monophosphates on *Mtb*PYK at sub-saturating substrate concentrations (Fig. 1). We consistently observed a significant PYK activation (over 3-fold increase in activity) by adding G6P in agreement with our previous findings [12]. Interestingly, instead of discovering another new activator, we found three inhibitors: R5P, ribulose 5-phosphate (5RP) and xylulose 5-phosphate (X5P). These pentose monophosphates from the pentose-phosphate pathway (PPP) share a highly similar chemical structure (Fig. 1a).

We then varied the concentrations of these three pentose monophosphates to investigate their role in *Mtb*PYK enzyme inhibition (Table 1). All three pentose phosphate inhibitors show sub-millimolar inhibition (IC_{50} = ~250–500 μM) that is comparable to the activation constant of G6P ($K_{a0.5}$ = ~150 μM) [12], where R5P is the most potent inhibitor with IC_{50} = 251 ± 24 μM. To test whether they share the same effector site with G6P, we added G6P (0.14 mM) to the assay and observed decreased inhibitory activity by R5P (IC_{50} increased from 251 to 407 μM), which is consistent with pentose monophosphate competing with G6P for binding to the same effector site, as we demonstrate in subsequent structural studies. We further performed detailed kinetic studies of *Mtb*PYK in the presence and absence of R5P, to evaluate the inhibitory mechanism. R5P decreased the apparent binding affinity of both substrates PEP and ADP, and slightly increased the cooperativity with respect to the substrate (*h*) (Table 1). In addition to changing the substrate binding affinity, R5P also decreased the maximum turnover number (k_{cat}) of the chemical reaction. Taken together, these results suggest that the pentose monophosphate is an uncompetitive inhibitor of *Mtb*PYK and indicate that this inhibitor

Table 1. Kinetic properties of *Mtb*PYK and the inhibitory effect of pentose monophosphate metabolites

Ligand	Kinetic parameter	Modulator	
		None	+R5P[a]
PEP	$S_{0.5}$ (mM)	0.41 ± 0.01[12]	0.53 ± 0.01
	Hill coefficient, *h*	1.8 ± 0.1[12]	2.0 ± 0.1
	k_{cat} (s^{-1})	183 ± 1.2[12]	133 ± 1.1
	$k_{cat}/S_{0.5}$ (s^{-1} mM^{-1})	446[12]	252
ADP	$S_{0.5}$ (mM)	0.40 ± 0.02	0.44 ± 0.03
	Hill coefficient, *h*	1.1 ± 0.1	1.3 ± 0.1
	k_{cat} (s^{-1})	165 ± 3.4	112 ± 2.5
	$k_{cat}/S_{0.5}$ ($s^{-1}\cdot mM^{-1}$)	412	255
		None	**+G6P**
R5P	IC_{50} (μM)	251 ± 24	407 ± 24
5RP	IC_{50} (μM)	407 ± 18	nd[b]
X5P	IC_{50} (μM)	530 ± 30	nd

[a] The concentrations of modulators are 2 mM for R5P and 0.14 mM for G6P.
[b] nd, not determined.

recognizes the substrate-bound conformation, thereby decreasing the progress of the enzymic reaction.

The pentose monophosphate R5P binds at the G6P site

We next used x-ray crystallography to determine the location of the R5P binding site on *Mtb*PYK. Efforts to co-crystallize R5P with *Mtb*PYK or to soak R5P into unligated *Mtb*PYK crystals were unsuccessful, and we were unable to obtain high-quality crystals for x-ray diffraction, suggesting that the binding of R5P to the inactive T-state enzyme is unfavorable. We previously encountered a similar problem when we tried to solve the AMP- or G6P-bound structures without oxalate (OX), which mimics the substrate and locks the enzyme in its active R-state conformation [12]. By soaking the R-state *Mtb*PYK crystal (active conformation in the presence of OX) with R5P, we were able to collect useful data and determined the structure at high resolution (Table 2). The R5P-bound *Mtb*PYK structure comprises a complete tetramer in the asymmetric unit. All three domains (A-domain, B-domain, and C-domain) of each subunit were well identified (Fig. 2a). The catalytic site is located in the cleft between A- and B-domains. The position of the B-domain is mainly regulated by the active-site ligands, and its open-closed transition may play a role in the enzyme reaction mechanism [15]. Two effector sites are located ~40 Å away from the catalytic site (Fig. 2b). One effector site is the canonical allosteric site in the C-domain that binds AMP for activating *Mtb*PYK. The other effector site, which involves domains A and C, binds the activator G6P as shown in our previous report [12] or the inhibitor R5P described in this study. Thus, this "sugar monophosphate site" is a unique "regulator-switching" site that could either "switch on" or "switch off" the PYK activity by the binding of different modulators.

Table 2. Data collection and refinement statistics

	*Mtb*PYK-OX/AMP/R5P
PDB ID	6ITO
Data collection	
Space group	$P3_1$
Cell dimensions	
a, *b*, *c* (Å)	125.55, 125.55, 143.82
α, *β*, *γ* (°)	90.00, 90.00, 120.00
Solvent content (%)	62
Resolution (Å)	62.77–2.55
No. of reflections	332,944 (18,516)
No. of unique reflections	82,657 (4510)
Wilson *B*-factor (Å^2)	38.9
R_{merge} (%)	12.4 (94.0)
$I/\sigma I$	8.8 (1.6)
Completeness (%)	100.0 (100.0)
Multiplicity	4.0 (4.1)
Refinement	
Monomers in ASU	4
No. reflections	78,503
R_{work}/R_{free}	0.2057/0.2476
No. of non-H atoms	
Protein	14,205
Water	540
Ligands	172
Average *B*-factor (Å^2)	
Protein	59.1
Water	46.8
Ligands	64.9
RMS deviations	
Bond lengths (Å)	0.0106
Bond angles (°)	1.2195
Ramachandran plots	
Favored (%)	96.6
Allowed (%)	99.6
Number of outliers	7

Values in parentheses are for the highest-resolution shell.

Clear electron density for the inhibitor R5P from each subunit is visible at the sugar monophosphate site (Fig. 2c). R5P is located in a similar position as the activator G6P (Fig. 2c, d; Fig. S2). Interestingly, R5P was found to be in an open-chain form in the crystal structure, which is different from the sugar-ring form of G6P identified in previous structures. Briefly, R5P is locked in place by salt bridges and hydrogen bonds (Fig. 2c, d; Fig. S2b). The phosphate of R5P forms salt bridges with two positively charged residues, Arg382 and Arg385 (both on helix 2 of the C-domain, Cα2), and hydrogen bonds with the "monophosphate loop" residues His345, Arg348, and Thr349. The pentose chain of R5P is hydrogen-bonded to Aα6 residues (Glu267, Asn268), the Cα2 residue (Arg382), and an additional water molecule. Note that Glu267 on Aα6 does not interact with G6P in the G6P-bound structure (Fig. 2c). Therefore, there is only a minor difference in binding mode between R5P and G6P at the sugar monophosphate site, which raises the question of why R5P is an inhibitor while G6P is an activator. We next explored the inhibitory mechanism by investigating the thermal stability and structural flexibility of *Mtb*PYK in the presence of R5P.

The pentose monophosphate R5P decreases the thermal stability and increases the dynamic movement of the B-domain

It has previously been shown that the binding of the active-site ligand oxalate triggers a conformational change (rigid-body rotation) of the *Mtb*PYK tetramer toward its active R-state (PDB ID: 5WS8) [12] and slightly stabilizes the enzyme in solution (ΔT_m = 0.3 °C) (Fig. 3a). The activator G6P further increased the thermal stability of R-state *Mtb*PYK by 1.7 °C, in agreement with our previous report [12]. In contrast to the thermal stabilization effect by the substrate analogue and the activator, the binding of inhibitor R5P slightly decreased the melting temperature of *Mtb*PYK (ΔT_m = −1.3 °C). Interestingly, the

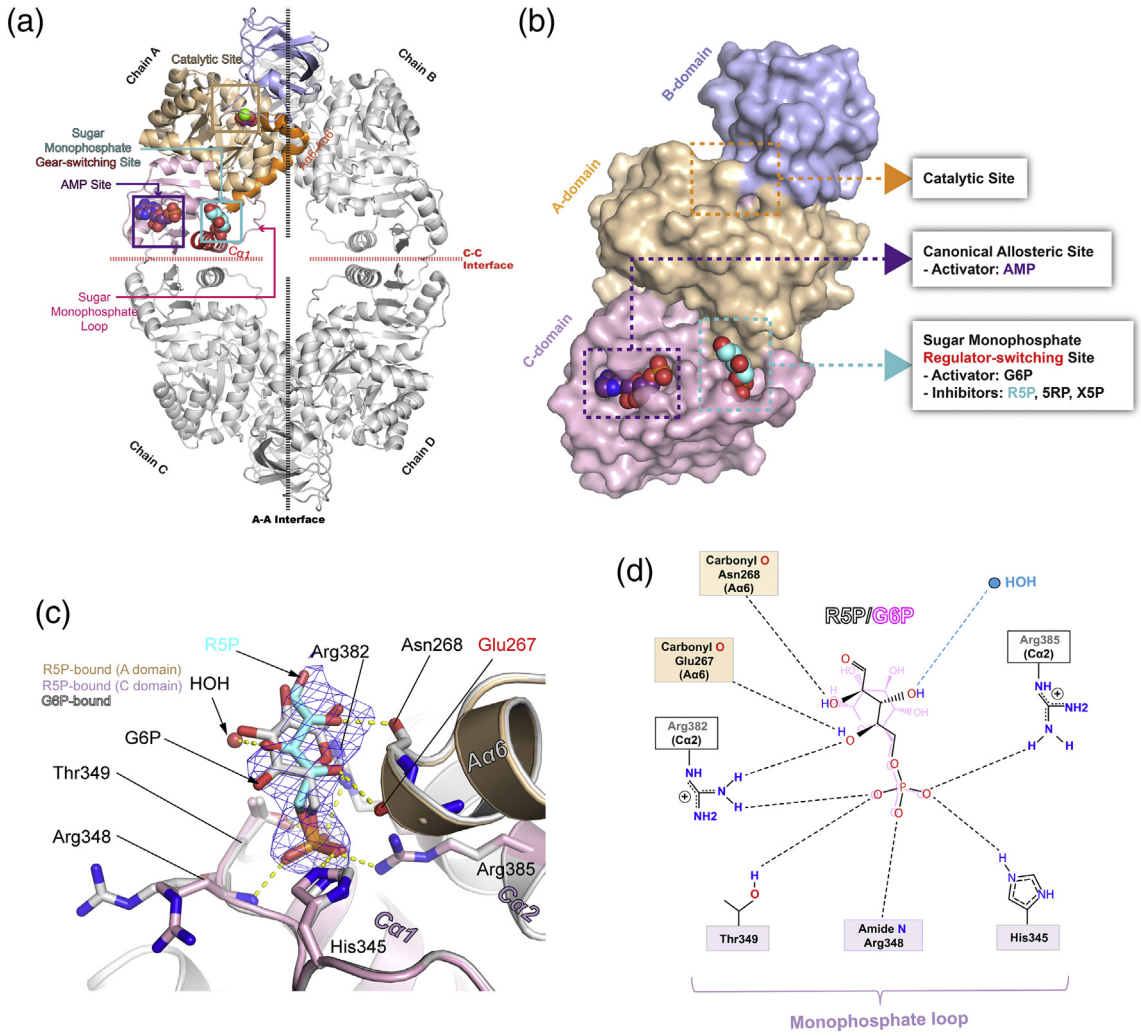

Fig. 2. The sugar monophosphate site regulates *Mtb*PYK activity by binding to either hexose monophosphate (activation) or pentose monophosphates (inhibition). (a) Overview of crystal structure of *Mtb*PYK tetramer. Each monomer comprises three domains shown in different colors. The polypeptide chains are shown as cartoons, while ligands are shown as spheres. Helices that are essential in the allosteric pathway are highlighted in red for Cα1 and orange for Aα6–Aα6′. (b) A surface representation of the *Mtb*PYK monomer (A-, B-, and C-domains) highlighting the catalytic site and two effector sites. Ligands are shown as spheres. (c) Close-up view of the superposed sugar monophosphate site highlighting the similar ligand binding modes. Structures *Mtb*PYK-OX/AMP/R5P (PDB ID: 6ITO) and *Mtb*PYK-OX/AMP/G6P (PDB ID: 5WSC) are superposed (C-α atoms fit) based on the AC-core (A- and C-domains) resulting in RMS fit of 0.23 Å. Ligand and interacting residues are shown as sticks, while a water molecule is shown as a red sphere. R5P is highlighted with an unbiased $F_o - F_c$ electron density map (blue) contoured at 3σ. Helices and the monophosphate loop that is involved in R5P binding are indicated. (d) A schematic representation showing the interatomic interactions at the sugar monophosphate site of the R5P-bound structure. R5P is superposed over the activator G6P to compare the binding mode.

product ATP, which normally decreases the dynamic movement of the B-domain [12,16], was able to partially reverse the effect of R5P (Fig. 3a), suggesting that the binding of R5P may be involved in the regulation of B-domain movement.

We next analyzed the B-domain motions in different ligated states of *Mtb*PYK. It is now well established that the lid-like B-domain has multiple conformations and that its closure movement toward the A-domain is initiated by the binding of active-site ligands including oxalate, PEP and ATP [15–17]. For example, oxalate binding causes the B-domains to rotate 11° toward the A-domain compared with the unligated form (Fig. 3b; Table S1 and Fig. S3). Also, additional interactions were formed to lock the B-domain in place when the B-domain was moving toward the A-domain (Table S2), leading to increased thermal stability [15]. Furthermore, we have shown that the B-domain regulator is not limited to ligands at the active site [12]. In *Mtb*PYK, allosteric

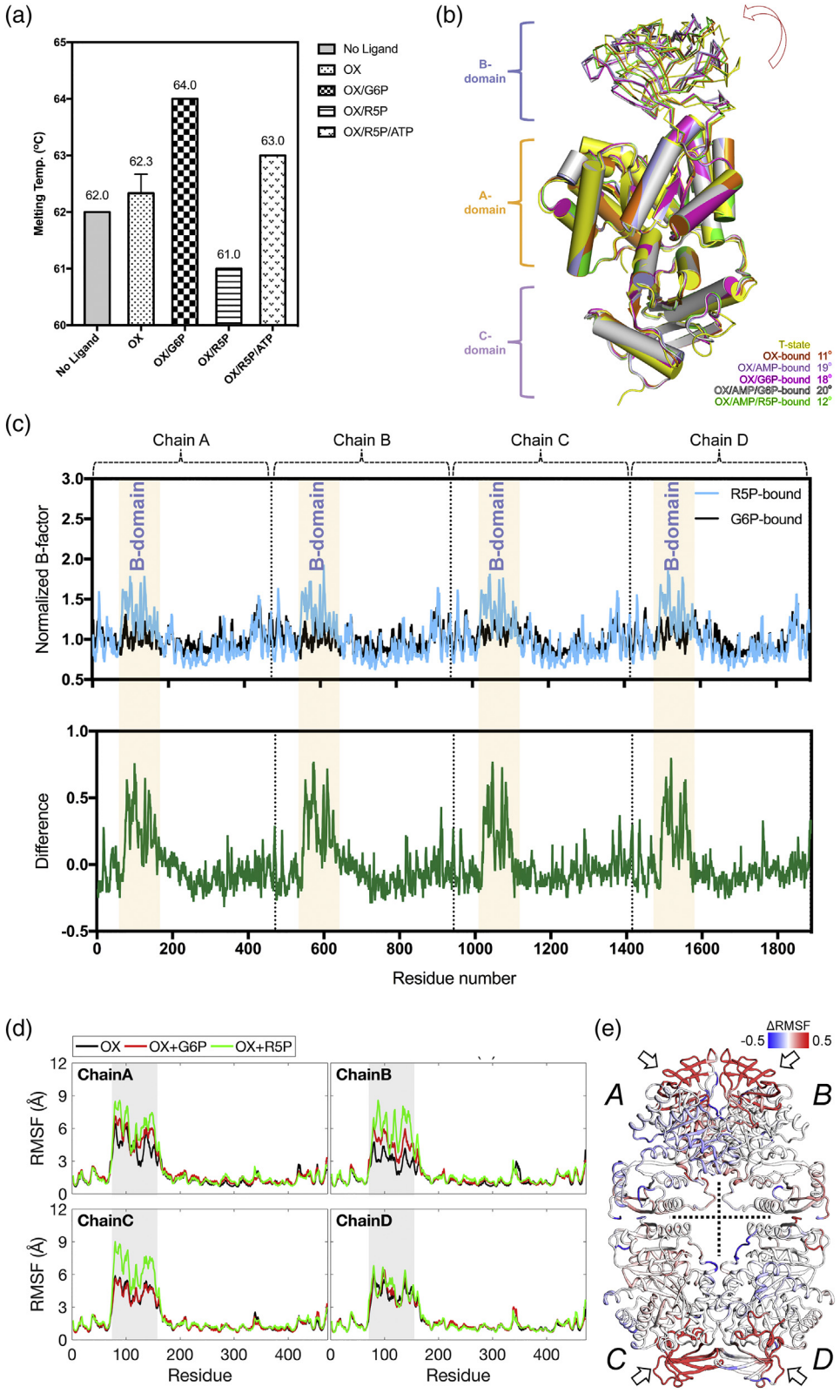

Fig. 3 (*legend on next page*)

activators (AMP and G6P) could also trigger the closure movement of the B-domain by a further 7–9° rotation (Fig. 3b), although the effector site is 40 Å away from the B-domain. Importantly, comparing the B-domain position of the R5P-bound structure with other *Mtb*PYK structures, we found that the inhibitor R5P did not facilitate the closure movement of the B-domain (only 1° difference) even in the presence of the activator AMP (Figs. 3b and S3). This finding is consistent with the thermal stability result where no stability enhancement was found upon R5P binding. The open conformation of the B-domain is normally associated with much higher fluctuations to domain positions.

To gain further insight into R5P effects on *Mtb*PYK, we examined the *B*-factor (temperature factor) parameter in x-ray crystallography, which has been widely used as an index of protein structural stability and residue flexibility [18]. Here we analyzed the normalized *B*-factors from R5P-bound (PDB ID: 6ITO) and G6P-bound (PDB ID: 5WSC) *Mtb*PYK structures. As shown in Fig. 3c, we observed higher *B*-factor values in the B-domains from the R5P-bound structure, which is consistent with the decrease in the thermal stability data (Fig. 3a). Together, our results show that the binding of R5P to *Mtb*PYK increases the dynamic movement of the B-domain, resulting in the observed higher crystallographic *B*-factor and contributing to the reduction of thermal stability. We next tested this model with MD simulations on the *Mtb*PYK tetramer to further investigate the role of R5P in *Mtb*PYK dynamics.

The MD of *Mtb*PYK

To gain new insight into the allostery of *Mtb*PYK upon ligand binding, we performed three independent 300-ns MD simulations for each of three systems (oxalate, oxalate + G6P, and oxalate + R5P; see Materials and Methods), which is more rigorous compared with previous measurements where only a 150-ns MD simulation was carried out [12]. First, the Cα root-mean-square-deviations (RMSDs) were calculated by superposing AC cores onto the starting crystal structure, to monitor the backbone fluctuations of *Mtb*PYK. As shown in Fig. S4, the RMSD values of the AC cores are stabilized around 4 Å, indicating that the core protein structure is well preserved among all systems, while highly fluctuating RMSDs show that the B-domains experience more dynamic movement. We then calculated the Cα root-mean-square-fluctuation (RMSF) of each residue over all runs and averaged these values to compare the backbone flexibility in detail (Fig. 3d). Consistent with the RMSD results, only the B-domain region (residues 71–167) shows high dynamic movement, while the remainder of the subunit is relatively rigid. From Fig. 3e, it is clear that the R5P system is more dynamic (indicated by the red color) than the G6P system, especially in the B-domains and the A–A and C–C interfaces. The binding of R5P also increases the dynamic movement of most of the sugar monophosphate loop compared with the binding of G6P, which might be propagated by the increased dynamics at the active site.

Both experimental data (Fig. 3a-c) and MD simulations (Fig. 3d) show that the binding of R5P increases the dynamic movement of the B-domain. In addition, the closure of B-domains toward the catalytic site, which stabilizes B-domains in position by additional interactions, is an essential feature of the active state [15,16]. Thus, it is important to understand the movement of the B-domain in simulations. Here, we calculated the Cα–Cα distances of residues in either the monomer or the dimer (along the short axis of the tetramer) of *Mtb*PYK, as a function of the presence of effector molecules (G6P and R5P). The differences are illustrated in Fig. S5. Within a monomer, G6P binding induces very small effects on the Cα–Cα distances. However, upon the binding of R5P, the B-domain moves away from the catalytic site (closer to

Fig. 3. R5P regulates the dynamic movement of the B-domain. (a) Thermal stability assay results show that R5P destabilizes *Mtb*PYK, while the activator G6P stabilizes the enzyme in the R-state (OX-bound). Adding ATP reduces the dynamic movement of the B-domain and thus increases thermal stability of the enzyme. The melting temperature T_m values (°C) are shown above the bars. All data are mean ± SEM for N = 3. (b) B-domain motions in different ligated states of *Mtb*PYK. Subunits from six *Mtb*PYK structures (chain D in each structure) are superposed based on the AC-core (A and C domains), thereby showing the movements (indicated by an arrow) of the B-domains: T-state *Mtb*PYK (PDB ID: 5WRP), *Mtb*PYK-OX (PDB ID: 5WS8), *Mtb*PYK-OX/AMP (PDB ID: 5WS9), *Mtb*PYK-OX/G6P (PDB ID: 5WSA), *Mtb*PYK-OX/AMP/G6P (PDB ID: 5WSC), *Mtb*PYK-OX/AMP/R5P (PDB ID: 6ITO). AC-cores are shown as cartoons, while the B-domains are represented by ribbons. The rotation angles of the B-domain relative to the T-state structure are indicated. The details of the B-domain positions are described in Table S1 and Fig. S3. (c) *B*-factor analysis of *Mtb*PYK tetramers indicates that the binding to R5P reduces the stability of the B-domain. The normalized *B*-factors (Å^2) of Cα atoms in the R5P-bound structure (light blue; PDB ID: 6ITO) and G6P-bound structure (black; PDB ID: 5WSC) are compared in the top panel. The bottom panel shows their difference in *Mtb*PYK: (normalized *B*-factors of Cα atoms in R5P-bound structure) – (normalized *B*-factors of Cα atoms in the G6P-bound structure). B-domains from the four chains (A, B, C, and D) in a tetramer are shaded in light yellow. (d) The backbone fluctuations in the absence and presence of allosteric ligands during the last 100 ns in MD simulation. The Cα RMSFs of individual residues in each system were plotted. (e) Differences in RMSFs of the R5P-bound form from those of the G6P-bound form are colored on the protein structure. Red and blue colors represent higher and lower flexibilities, respectively. A–A and C–C interfaces are indicated by dashed lines. B-domains are indicated by arrows.

residues 1–70 and 168–215 in the A-domain). Hence, a twisting of the B-domain is observed instead of a closure motion toward the catalytic site (Fig. S5a, b). For the dimer, in the presence of R5P, the B-domain in one monomer moves far away from the other monomer, indicating a more open conformation of the B-domains (Fig. S5c, d). Thus, although the allosteric site is ~40 Å away from the B-domain, binding of G6P or R5P there has obvious but distinctly different effects on both the dynamics and conformations of the B-domains. Together, the MD simulations agree with the preceding findings from thermal stability assays (Fig. 3a) and crystal structures (Fig. 3b and c), showing that the inhibitor R5P increases the protein structure flexibility and hinders the B-domain closure movement toward the catalytic site.

In addition, the three simulation systems show distinct binding stabilities of small molecules (oxalate and G6P/R5P) based on their heavy-atom RMSDs (Figs. S6 and S7). The smallest fluctuations of RMSDs were observed in the oxalate + G6P system for both oxalate and G6P, indicating their high binding stabilities. However, the binding of ligands in the oxalate + R5P system showed greater fluctuation. Therefore, the stable binding of G6P in the allosteric site enhances the binding of oxalate in the active site, while the relatively weak contact with R5P decreases its binding. Consistent with the biochemical results (Table 1; Fig. 1b), G6P and R5P induce opposite allosteric effects propagating from the allosteric site to the active site. Compared to an open-chain conformation of R5P, the rigid ring of G6P markedly increases the steric hindrance and reduces the degree of freedom of the small molecule. This might be the reason for the less "dynamic" binding of G6P than R5P (Fig. S7). We next explored the community networks and allosteric pathways to further understand the inhibitory mechanism of R5P.

Strengthened *versus* weakened intra- and inter-domain coupling through similar allosteric pathways

In MD simulations, a protein can be partitioned into communities based on physical contacts between residues and their positional correlation. Residues within communities form dense contacts, while forming sparse contacts between communities. Widely used in allosteric studies [19], community analysis is an effective way to reveal the pattern of motional coupling within a protein, so we used it here to further define the effects of G6P and R5P binding on *Mtb*PYK. As shown in Fig. 4a–b, in the presence of G6P, residue coupling within *Mtb*PYK is quite strong, leading to a dense and stable interaction network, which can promote efficient allosteric communication. Each monomer is partitioned into three communities upon G6P binding, mainly corresponding to the A-, B-, and C-domains. However, when replacing G6P with R5P, domain A or community A is broken up into two communities, A and A′ (Fig. 4c–d). Moreover, the inter-community connections are also weakened, indicating the weaker strength of coupling in the presence of R5P. Hence, a more localized and lower cooperative allosteric network is observed upon R5P binding.

To further explore the molecular basis of the opposite allosteric effects induced by G6P and R5P, potential allosteric pathways were identified between oxalate in the catalytic site and G6P/R5P in the sugar monophosphate site (referred to as OX–G6P and OX–R5P). A set of key residues with a high frequency of occurrence was identified from all the observed allosteric pathways. As illustrated in Fig. 4e–f, the key residues in OX–G6P and OX–R5P pathways are located in similar regions of the protein, sharing six residues of the top 10 of each: Ile216, Lys218, Asp244, Arg242, Glu267, and Asn268 (Fig. 4e). The OX–G6P pathway identified here is consistent with our previous simulation results [12]. Moreover, residues that occur the most often in the OX–G6P paths are more centralized than in the OX–R5P paths, which might be due to the higher flexibility of the R5P system. Indeed, the optimal path is found to be slightly shorter in the OX–G6P paths. Interestingly, the residues exclusive to the OX–G6P path (Val232, Phe235 and Ala265) are hydrophobic residues, as well as the shared residue Ile216, so there is a consistent hydrophobic core in the middle of the OX–G6P pathway. Similar to the peptide that induces inter-domain allosteric communication in a peptidyl-prolyl cis/trans isomerase pin1 [20], G6P might serve as a bridge linking the A- and C-domains, and hence, its binding stabilizes the conformation of the allosteric site, especially the allosteric loop (monophosphate loop). Although R5P binds at the same site, its high dynamics make its binding less stable than G6P, which might amplify the protein dynamics from the sugar monophosphate loop to both the A–A (through helices Aα6–Aα6′) and C–C interfaces (through Cα1) (Fig. 2a). In addition, the hydrophobic core at the top of the allosteric site in the A-domain suggested by the pathway analysis might also be disturbed, which may further decrease oxalate binding in the catalytic site.

Positive *versus* negative allosteric regulation from the same site by fine-tuning of the conformational dynamics

Some reports have shown that tight binding of ligands can enhance residue coupling and further induce proteins to become more rigid and dense, especially around the binding site [19–21]. This reduction in conformational dynamics has been

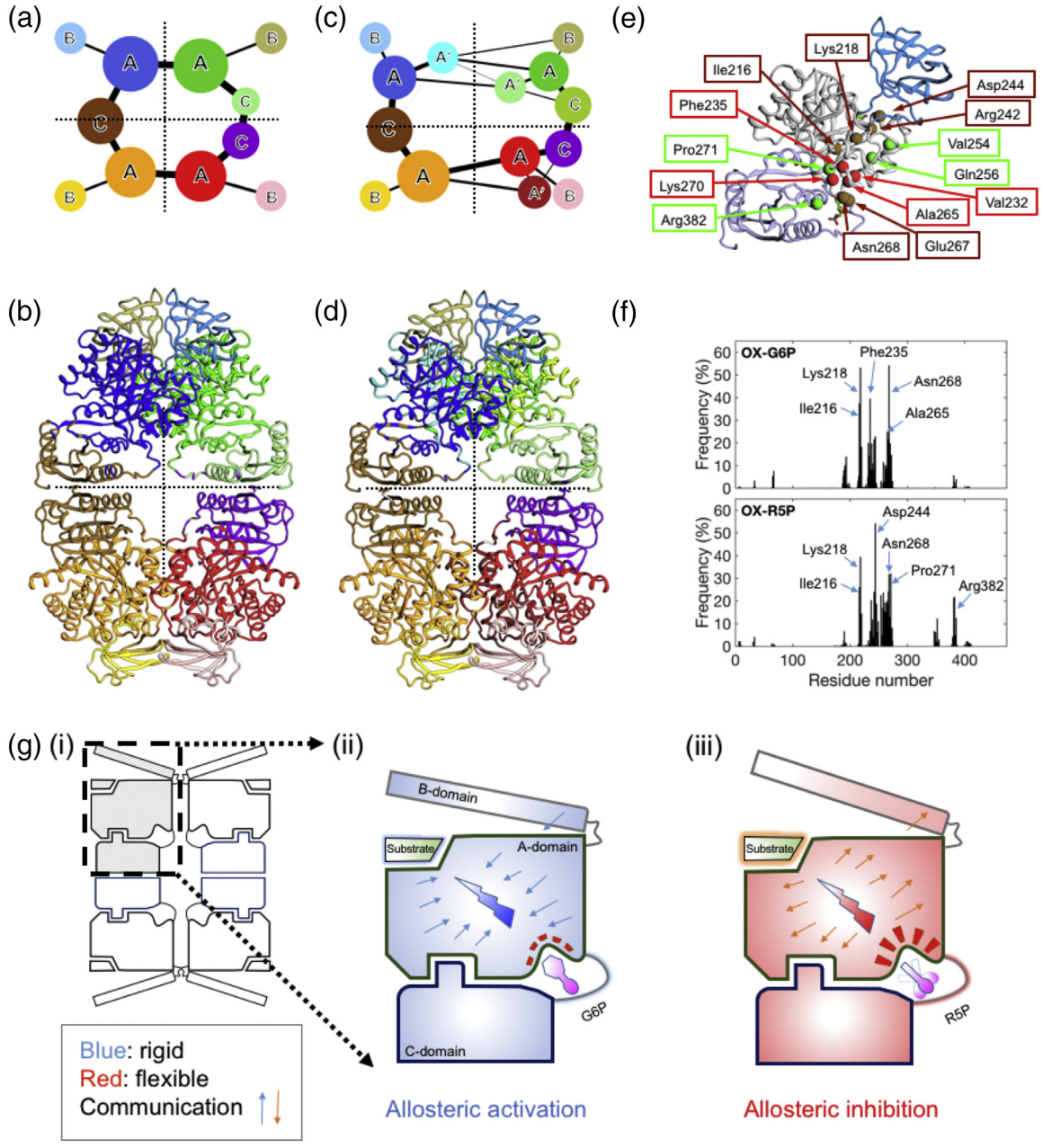

Fig. 4. Community and allosteric pathway analysis. (a, b) Communities of the G6P-bound *Mtb*PYK system. (c, d) Communities of the R5P-bound *Mtb*PYK system. On the top, the communities represented by circles are connected by inter-community edges, and the edge width is proportional to the cumulative betweenness. The corresponding structures (bottom) are shown in cartoon colored by community. (e) Key residues involved in the allosteric pathways between the catalytic site and the sugar monophosphate site. The top 10 residues in each pathway are shown as spheres, and the protein is drawn in ribbon, with A-, B-, and C- domains in silver, blue, and light purple, respectively. The shared portion of the key residues is colored in ochre. Residues unique in OX–G6P pathways are in red, and those unique in OX–R5P pathways are in green. (f) The frequency of residues involved all recognized pathways. Top residues identified from the pathway analysis are indicated. (g) Illustration of the positive (ii) and negative (iii) allosteric regulation mechanisms of *Mtb*PYK by G6P and R5P, respectively. Schematic representations of *Mtb*PYK tetramer (i) and monomer are shown, where domains, ligands and loops are indicated. The allosteric effects propagate from the allosteric site to the catalytic centre through pathways. The changes in dynamics and the allosteric coupling are indicated by arrows and colored in either blue or red. G6P represents tight binding ligands in positive allosteric regulation (blue), while R5P corresponds to relatively weaker binding of allosteric inhibitors (red).

observed in many positive allosteric modulations [19,20]. Interestingly, the less common negative allostery is often accompanied by the increase of conformational dynamics [21].

As shown in Figs. 3 and 4, the two allosteric effectors in this study bind to an identical site but induce distinct effects: G6P decreases protein flexibility and strengthens allosteric coupling, but R5P enhances the dynamics of the protein and weakens the internal communication. Based on our simulations, we speculate that, as the dominant allosteric pathways are similar for OX–G6P and OX–R5P, the opposite allosteric effects on the active site might be due to the opposing propagated signals of

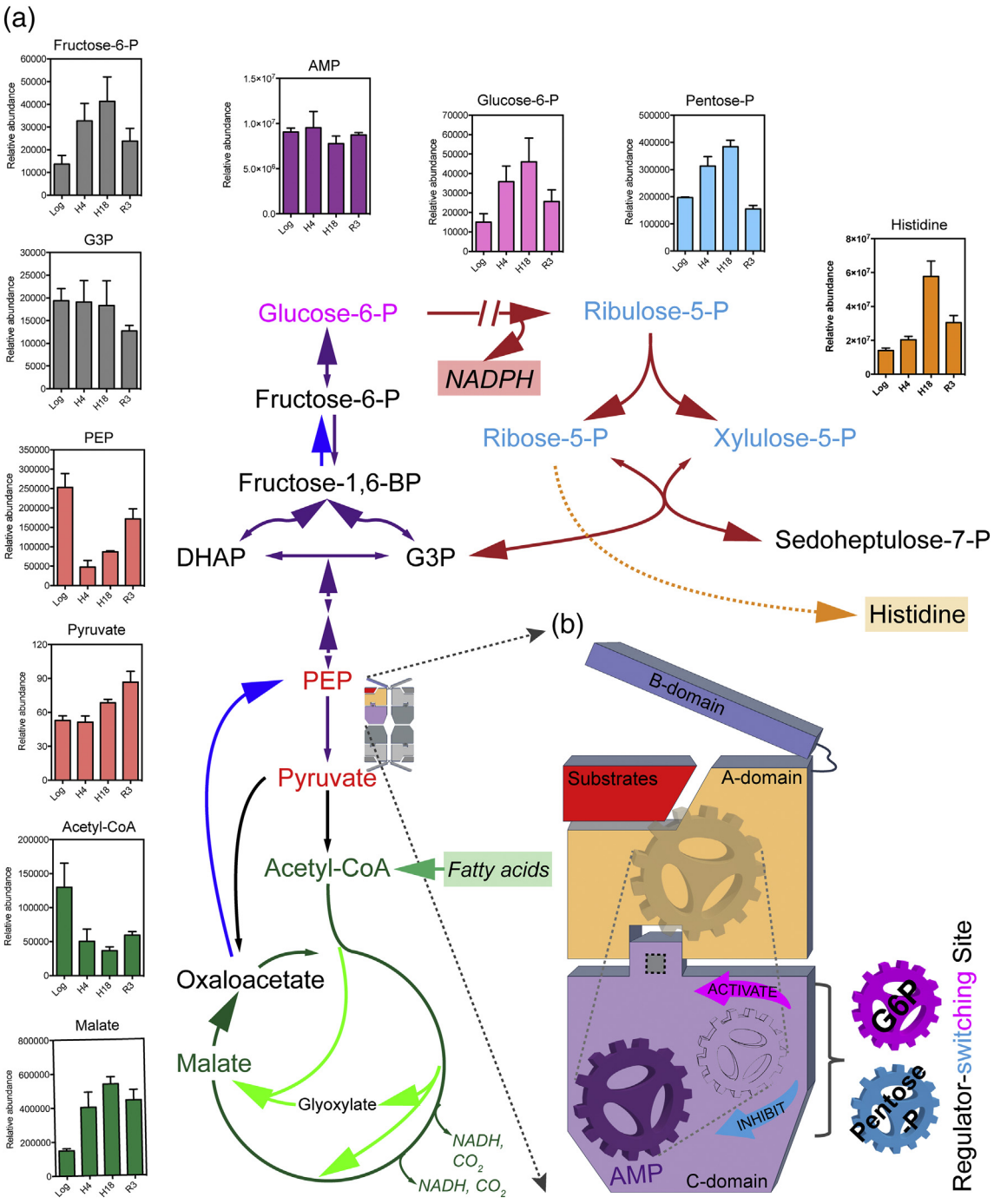

Fig. 5 (*legend on next page*)

fine-tuned protein flexibility. In contrast to the conventional positive allosteric effectors shown in Fig. 4g(ii), the binding of allosteric inhibitors might disturb the intrinsic coupling and therefore propagate a reduced residue–residue communication and increased protein conformational dynamics to the active site [Fig. 4g(iii)]. This may in turn promote the higher rates of substrate dissociation and the decreased substrate affinity. With this complex allosteric mechanism driven by conformational dynamics, *Mtb*PYK may sense different metabolites and react to stress-induced metabolic changes in *M. tuberculosis* cells as an adaptive response, as will be established in the next section.

PYK facilitates the remodeling of carbon flux distribution toward the PPP *in vivo*

We next sought to place the complex allosteric mechanism of *Mtb*PYK in the context of metabolic remodeling in mycobacteria. To understand the metabolic regulation and the carbon flux distribution around the PEP–pyruvate–oxaloacetate node in response to hypoxia, we subjected the well-characterized Mtb surrogate, *M. bovis* BCG [11,22,23], to hypoxic stress and applied chromatography-coupled tandem quadrupole mass spectrometry (LC–MS/MS) to quantify changes in the levels of relevant CCM intermediates. As shown in Fig. 5a, hypoxia increased pentose-phosphate levels (R5P, 5RP, and X5P) at 4 and 18 days (H4 and H18). After 3 days of reaeration (R3), pentose-phosphate levels shifted back to similar concentrations found in logarithmic growth. The finding that PPP intermediates accumulate is consistent with the work of Eoh and colleagues [9] using a different hypoxia model. We also observed an increase in histidine levels that correlated well with the R5P accumulation, which is reasonable since R5P is the core precursor for the synthesis of histidine. In contrast, most of the intermediates in the upstream steps of glycolysis were up-regulated, including G6P and fructose 6-phosphate (F6P), while the levels of downstream intermediates such as glyceraldehyde 3-phosphate (G3P) and PEP were reduced (Fig. 5a). Interestingly, only a small increase in the level of pyruvate was observed at the late stage of hypoxia (H18), suggesting that the flux toward the TCA cycle from pyruvate was relatively slow during hypoxia. In addition, hypoxia caused a sharp increase in malate in the TCA cycle and the reduction of acetyl-CoA, resulting from the up-regulation of the glyoxylate shunt for the demands of gluconeogenesis under hypoxic stress [24,25]. The glyoxylate shunt, bypassing the two carbon dioxide-generating steps of the TCA cycle, is known to be essential for using fatty acids as carbon sources under physiological conditions requiring gluconeogenesis [24–26].

In contrast to the dramatic increase in AMP levels in nutrient deprivation [12], with AMP as a positive regulator of *Mtb*PYK activity, hypoxia did not cause a notable change in levels of AMP (Fig. 5a), which points to a less important role for AMP regulation of *Mtb*PYK activity in hypoxia. This suggests that the other two modulators, R5P and G6P, which show appreciable changes during hypoxia, are responsible for regulating *Mtb*PYK activity in response to hypoxic stress.

Discussion

The sugar monophosphate site in *Mtb*PYK provides the enzyme with a unique competitive allosteric mechanism—a conformational dynamics-driven regulatory system that delivers a switching system to decelerate or accelerate the reaction rate to meet the metabolic demands during the cell stress response (Fig. 5b), depending on the relative concentrations of R5P (inhibitor) and G6P (activator) in cells. It has been reported that the intracellular concentrations of pentose monophosphates and G6P in bacteria (*Escherichia coli*) are in the millimolar range [27–30], further suggesting that changes of relative concentrations of pentose monophosphates and G6P could play a key role in PYK activity regulation at different growth stages of mycobacteria. The metabolic profiling results suggest that the carbon flux was directed to the PPP by the glyoxylate shunt and gluconeogenesis in response to the adaptation of mycobacteria to hypoxia. Thus, keeping the

Fig. 5. A conformational dynamics-driven allostery regulates pyruvate kinase activity to fine-tune metabolism and control redox homeostasis in *M. tuberculosis*. (a) Schematic illustration of glycolysis, pentose-phosphate pathway, TCA cycle, glyoxylate shunt, and histidine synthesis in *M. bovis* BCG. The bigger arrows indicate the increased fluxes during hypoxia. Histograms of metabolic changes at H4, H18, and R3 against Log in *M. bovis* hypoxia model; abundance data represent mean ± SEM, N = 3. Polysorbate 80 served as a fatty acid surrogate in this hypoxia model. (b) A three-dimensional (3D) representation of *Mtb*PYK with a "regulator-switching" system for differential transmission of allosteric inhibition and activation signals. One subunit of *Mtb*PYK tetramer is highlighted showing the catalytic site comprised of the A-domain (beige) and B-domain (blue box at top), and C-domain allosteric site (light purple at bottom). The metabolites Pentose-P (ribose-5-P, ribulose-5-P, xylulose-5-P), glucose-6-P (G6P), and AMP are shown as gears colored in blue, magenta, and purple, respectively. The sugar monophosphate site in the C-domain is represented by the transparent "effector" gear that switches between inhibition by Pentose-P and activation by G6P. These regulatory signals are transmitted (dashed lines) to the catalytic site (gear in A-domain). When AMP levels do not change, the "effector" engages the A-domain to regulate catalytic inhibition and activation by Pentose-P and G6P, respectively.

glycolytic PYK at a relatively low activity is necessary to prevent the reverse flow of carbon through the glycolytic pathway to the TCA cycle. In agreement with this model, we have observed the stress-induced increase of pentose phosphates that could serve as *Mtb*PYK inhibitors, to presumably decelerate the carbon flow through PYK and subsequently change the carbon flux distribution at the PEP–pyruvate–oxaloacetate node. It is noteworthy that hypoxia also induced an increase in the activator G6P simultaneously, further suggesting that the PYK activity is finely tuned by minute-to-minute changes in the relative concentrations of R5P and G6P. To our knowledge, this is the first demonstration that in bacteria, PYK uses one single allosteric site to accommodate opposing-effect modulators for facilitating metabolic reprograming. This regulatory mechanism has recently been reported for human M2PYK (namely "allostatic" regulation) as a finely balanced feedback mechanism in cancer development [13].

What are the physiological consequences in mycobacteria of up-regulating the glyoxylate shunt and increasing the carbon flux to the PPP during hypoxia? Exposure to hypoxia seems to result in a lower rate of glycolysis and a relatively higher glyoxylate shunt and gluconeogenesis activity that overcome glycolysis and reroute the flow of carbon to the PPP. The accumulation of metabolic intermediates during hypoxia was shown by Eoh and colleagues [9] to be the result of an anticipatory metabolic regulatory response, required by *M. tuberculosis* for cell cycle re-entry.

Another potential physiological consequence of elevating the PPP flux is for redox balance (antioxidant response), which is also found in human cancer M2PYK through posttranslational modification [14,31]. When bacterial cells encounter hypoxia, the redox potential will drop due to insufficient terminal electron acceptors for the respiratory chain. Thereafter, electron carriers of the chain become saturated and electrons "leaking" from the chain may directly react with the small amounts of remaining oxygen to generate radicals (ROS) and cause damage [32–35]. NADPH (a major product of the PPP) is required to generate sufficient reducing potential for detoxification of ROS and to repair the damage [36]. Thus, in this work, we have demonstrated that mammalian and bacterial PYKs have evolved alternative ways of regulating PPP for detoxification, where human M2PYK senses ROS [14] and mycobacterial PYK uses a unique competitive allosteric mechanism of sensing sugar monophosphates.

In addition, bypassing the carbon dioxide-generating steps of the TCA cycle where part of the cellular NADH pool is regenerated could prevent the overloading of reduced electron carriers funneled into respiration when oxygen is limited during hypoxia [24,32]. Therefore, this complex but sensitive allosteric scheme provides PYK with an efficient mechanism for helping *M. tuberculosis* to fine-tune metabolism and detoxification in response to hypoxia.

Materials and Methods

Expression and purification of *Mtb*PYK

A codon-optimized *Mtb*PYK gene (Bio Basic Inc.) was cloned into a pYUB28b-TEV vector (N-terminal His_6-tag followed by the TEV protease cleavage site) and the plasmid was used to transform chemically competent *E. coli* BL21(DE3) cells (Novagen, Merck Millipore). *Mtb*PYK protein was overexpressed and purified as described previously [12].

*Mtb*PYK kinetics and inhibition assays

PYK activity was measured at 25 °C by following NADH consumption as a decrease in absorbance at 340 nm using a microplate reader BioTek Synergy 4. To determine the inhibitory effect of pentose monophosphates on *Mtb*PYK, enzyme activity and kinetics were determined as described previously [12] but in the presence of 2 mM inhibitor R5P. The data were analyzed by the software Graphpad Prism 7. The PYK inhibition assay was performed at 25 °C in 100 µl reaction mixtures containing 1× assay buffer [50 mM triethanolamine (pH 7.2), 100 mM KCl, 10 mM $MgCl_2$], 0.2 mM ADP, 0.2 mM PEP, 0.5 mM NADH, 3.2 U L-lactate dehydrogenase (LDH), and 1.6 µg ml^{-1} *Mtb*PYK. *Mtb*PYK enzyme in 1× assay buffer was pre-incubated with the inhibitor (R5P, 5RP, or X5P) in a serial dilution at ambient temperature for 10 min. The negative control mix was made up in an identical manner, except that 1× assay buffer was used in place of the inhibitor solution. To test the interplay between G6P and pentose phosphates on *Mtb*PYK activity, we also carried out the inhibition assay for R5P in the presence of 0.14 mM G6P. The IC_{50} values for each inhibitor were estimated by expressing the reaction rate for each activity assay with a series of inhibitor concentrations as a percentage of the control assay and analyzing the data using nonlinear regression fit in Graphpad Prism 7. All kinetics and inhibition results are summarized in Table 1.

Thermal stability assay

The thermal stability analysis of *Mtb*PYK was performed as described previously [12]. Briefly, 4 µM *Mtb*PYK enzyme was pre-incubated for 10 min with 5 mM of the test ligand(s) (oxalate, ATP, G6P, R5P) in a 96-well PCR plate (Bio-Rad) in

assay buffer consisting of 50 mM triethanolamine (pH 7.2), 100 mM KCl, 10 mM $MgCl_2$. After incubation, 5× SYPRO Orange dye (Invitrogen) was added to make a final volume of 50 µl per reaction. The changes of fluorescence with increasing temperature ranging from 25 to 95 °C were monitored in the i-Cycler iQ5 real-time PCR system (Bio-Rad). The temperature midpoint T_m for the protein-unfolding transition was calculated using the Bio-Rad iQ5 software.

Crystallization and data collection

Crystals of *Mtb*PYK complexed with oxalate (OX) were grown by the vapor-diffusion method using the hanging-drop technique at 4 °C as described previously [12]. Briefly, crystals were grown in the solution consisting of 12% PEG 8000, 20% glycerol, 50 mM triethanolamine, 100 mM KCl, 50 mM $MgCl_2$, and 5 mM OX (pH 7.2). To obtain the R5P-bound structure, *Mtb*PYK-OX crystals were soaked with a mixture of 5 mM each of AMP and R5P in 20% PEG 8000 and 20% glycerol. Although we attempted to soak R5P into crystals of unligated *Mtb*PYK (T-state), the crystals did not diffract well after soaking. X-ray intensity data for the crystal of *Mtb*PYK-OX/AMP/R5P were collected at the Swiss Light source (SLS, Switzerland). The data set was from a single crystal flash-cooled in liquid nitrogen at 100 K. Data were processed with MOSFLM [37] and scaled with AIMLESS [38,39]. The data collection and processing statistics are summarized in Table 2.

Structure determination

The *Mtb*PYK-OX/AMP/R5P structure was solved by molecular replacement using the program Phaser [40]. The initial search model for the molecular-replacement experiment was obtained from the published structure *Mtb*PYK-OX/AMP/G6P (PDB ID: 5WSC). The structure was manually adjusted using Coot [41] followed by several cycles of restrained refinement in REFMAC [42]. Where appropriate, water molecules and ligands were added to the structure and TLS refinement was applied at a later stage of refinement. The quality of the structures was assessed using the MOLPROBITY server [43], and the figures were generated using PyMOL [44]. The data processing and refinement statistics are summarized in Table 2. The structure factor and coordinates for *Mtb*PYK-OX/AMP/R5P have been deposited in the RCSB Protein Data Bank as PDB entry 6ITO.

MD simulations and community network analysis

Three systems of *Mtb*PYK were simulated in this study: OX, OX + G6P, and OX + R5P. All models with Mg^{2+} in the active site were prepared based on the crystal structure of *Mtb*PYK in complex with oxalate and G6P [12] (PDB ID: 5wsa), while the coordinates of R5P were taken from the complex with oxalate and R5P (PDB ID: 6ITO). All simulations were carried out using the AMBER 16 software [45] together with the AMBER14SB force field. The force field parameters for OX, R5P, and G6P were generated using the general AMBER force field (GAFF) in the Antechamber suite.

Each complex was solvated in a cubic box with TIP3P waters [44], with an at least 10-Å distance between the solute and the edge of the box. Sodium ions were added to neutralize the system. The whole system was first energy minimized, with a series of position restraints on the solute (all heavy atoms, backbone atoms and ligands, Cα atoms and ligands). The simulation was continued for 300 ns at 1 bar (maintained by isotropic position scaling with a 2-ps relaxation time) and 298.15 K (using the Langevin thermostat with a 2-ps^{-1} collision frequency). The SHAKE algorithm [46] was used to constrain all bonds involving hydrogens, allowing for a 2-fs timestep. Electrostatic interactions were treated by the particle mesh Ewald sum method [47], with a 8-Å cutoff for non-bonded interactions in direct space. Each system was simulated for three replicas.

The CPPTRAJ tool [48] was used for RMSD, RMSF, and Cα–Cα distance calculations. The community network analysis was performed using the NetworkView plugin in VMD [48] with the default setting. The last 100 ns was used for analysis.

M. bovis BCG culture and *in vitro* hypoxia model

A well-defined and highly reproducible adaptation of the Wayne Model was used to induce hypoxic conditions in *M. bovis* BCG cultures [11,22,23]. Each replicate uses an inoculum prepared from a single colony picked from 7H11 agar plates and pre-cultured in 7H9 media in roller bottles, rotated at 50 rpm, for up to 14 days at 37 °C. Optical densities at 600 nm (OD_{600}) were monitored daily and cultures at mid-log phase ($0.4 < OD_{600} < 0.8$) were either harvested (day 0) or diluted to an OD_{600} of 0.05 in Dubos medium (supplemented with Dubos Medium Albumin and Polysorbate 80). Polysorbate 80 served as the carbon source for growth of mycobacteria. Non-replicating *M. bovis* BCG cultures were produced by subjecting bacilli to hypoxia caused by gradual oxygen consumption in sealed bottles, as previously described [11]. Briefly, aerobic cultures (780 ml) with an initial OD_{600} of 0.005 were expanded in glass bottles with a capacity of 1000 ml (Duran, Wertheim, Germany), achieving an optimal headspace ratio (HSR) as previously specified [49]. The sealed cultures were stirred gently at 80 rpm for up to 18 days to allow the bacilli to enter into a non-replicating state on a self-

generated oxygen gradient. Subsequently, the select hypoxic cultures were reoxygenated by inoculating them into Erlenmeyer flasks containing fresh Dubos medium and shaking them on an orbital shaker at 140 rpm for up to 3 days. Oxygen depletion in these cultures was monitored by methylene blue coloration. Growth and survival were monitored by enumeration of colony-forming units (CFUs) on Middlebrook 7H11 agar after a 4 week incubation at 37 °C.

Metabolite extraction and metabolic profiling

Metabolite extraction and targeted metabolomics analyses followed published reports with modifications [12,50]. Briefly, *M. bovis* BCG cell cultures were harvested at various times, rapidly quenched on ice and spun down. Cell pellets were resuspended in acetonitrile/methanol/water (2:2:1) and lysed mechanically with 0.1-mm silica beads by using QIAGEN TissueLyser II. The lysates were collected and evaporated to dryness in a vacuum evaporator, and the dried extracts were redissolved in 100 µl of 98:2 water/methanol for LC–MS/MS analysis.

The targeted LC–MS/MS analysis was performed with Agilent 1290 ultrahigh-pressure liquid chromatography system coupled to a 6490 Triple Quadrupole mass spectrometer equipped with a dual-spray electrospray ionization source (Agilent Technologies, Santa Clara, CA). Chromatographic separation of glycolysis intermediates was achieved by using a Rezex ROA-Organic Acid H+ (8%) column (2.1 × 100 mm, 3 µm; Phenomenex, Torrance, CA), and the compounds were eluted at 40 °C with an isocratic flow rate of 0.3 ml min^{-1} of 0.1% formic acid in water. Compounds were quantified in multiple-reaction monitoring (MRM) mode with the following transitions: *m/z* 259 → 199 for glucose 6-phosphate (G6P), *m/z* 259 → 169 for fructose 6-phosphate (F6P), *m/z* 87 → 43.1 and *m/z* 87 → 32.1 for pyruvate, *m/z* 167 → 79 and *m/z* 167 → 63 for phosphoenolpyruvic acid (PEP), *m/z* 169 → 97 and *m/z* 169 → 79 for glyceraldehyde 3-phosphate (G3P), *m/z* 229 → 97 and *m/z* 229 → 79 for the pentose-phosphate pool (ribulose 5-phosphate, ribose 5-phosphate, and xylulose 5-phosphate), *m/z* 810 → 428 and *m/z* 810 → 303 for acetyl-CoA, and *m/z* 133 → 115 and *m/z* 133 → 71 for malic acid. AMP was analyzed using an Agilent rapid resolution HT Zorbax SB-C18 column (2.1 × 50 mm, 1.8 mm; Agilent Technologies) with the transition of *m/z* 348 → 136. The gradient elution involved a mobile phase consisting of (A) 0.1% formic acid in water and (B) 0.1% formic acid in methanol. The initial condition was set at 2% B, which was held for 3 min. A 2-min linear gradient to 95% B was applied, which was held for 3 min, then returned to starting conditions over 0.1 min. Histidine was analyzed using an Atlantis HILIC column (2.1 × 100 mm, 1.7 µm; Waters, Eschborn, Germany) with the transition of *m/z* 348 → 136. The gradient elution involved a mobile phase consisting of (A) 10 mM ammonium formate and 0.1% formic acid in water and (B) 0.1% formic acid in acetonitrile. The initial condition was set at 100% B for 2 min, followed by a linear gradient to 80% B over 11 min and then down to 40% B over 1 min, which was held for 5 min. Then the gradient returned to starting conditions over 1 min. The auto-sampler was cooled at 4 °C, and an injection volume of 5 µl was used for all the analyses. Electrospray ionization was performed in both positive and negative ion modes with the following source parameters: drying gas temperature, 300 °C with a flow of 10 l min^{-1}; nebulizer gas pressure, 40 psi; sheath gas temperature, 350 °C with a flow of 11 l min^{-1}; nozzle voltage, 500 V; and capillary voltage, 4000 and 3000 V for positive and negative modes, respectively. Data acquisition and processing were performed using MassHunter software (Agilent Technologies), and total peak area normalization was performed to correct for variations in sample preparation.

Untargeted metabolomics were performed as previously described to obtain total peak area [51]. The redissolved dry extracts were analyzed using an Agilent 1290 ultrahigh-pressure liquid chromatography system equipped with a 6520 QTOF mass detector managed by a MassHunter workstation. The column used for the separation was an Agilent rapid resolution HT Zorbax SB-C18 column (2.1 × 100 mm, 1.8 µm; Agilent Technologies). The oven temperature was set at 45 °C. The gradient elution involved a mobile phase consisting of (A) 0.1% formic acid in water and (B) 0.1% formic acid in methanol. The initial condition was set at 5% B. A 7-min linear gradient to 70% B was applied, followed by a 12-min gradient to 100% B, which was held for 3 min, then returned to starting conditions over 0.1 min. The flow rate was set at 0.4 ml min^{-1}, and 5 ml of samples was injected. The electrospray ionization mass spectra were acquired in positive ion mode. Mass data were collected between *m/z* 100 and 1000 at a rate of two scans per second. The ion spray voltage was set at 4000 V, and the heated capillary temperature was maintained at 350 °C. The drying gas and nebulizer nitrogen gas flow rates were 12.0 l min^{-1} and 50 psi. Two reference masses were continuously infused to the system to allow for constant mass correction during the run: *m/z* 121.0509 ($C_5H_4N_4$) and *m/z* 922.0098 ($C_{18}H_{18}O_6N_3P_3F_{24}$). Raw spectrometric data were analyzed by MassHunter Qualitative Analysis software (Agilent Technologies), and the molecular features characterized by retention time (RT), chromatographic peak intensity, and accurate mass were obtained by using the Molecular Feature Extractor algorithm. The features were then analyzed by MassHunter Mass Profiler Professional software (Agilent Technologies). Only features with an intensity ≥20,000 counts (approximately three times the limit of

detection of our LC–MS instrument) and found in at least 80% of the samples at the same sampling time point signal were kept for further processing. A tolerance window of 0.15 min and 2 mDa was used for alignment of RT and *m*/*z* values.

Accession numbers

Coordinates and structure factors for *Mtb*PYK-OX/AMP/R5P have been deposited in the Protein Data Bank under the accession code 6ITO.

Acknowledgments

The MD simulations were performed on the National Supercomputing Centre, Singapore. We are grateful to Dr. Ghader Bashiri from The University of Auckland (New Zealand) for the gift of the vector pYUB28b. This research was supported by the National Research Foundation of Singapore through the Singapore–MIT Alliance for Research and Technology Antimicrobial Resistance research program, and a Singapore–MIT Alliance for Research and Technology Postdoctoral Fellowship (W.Z.). During the course of this study, the J.L. laboratory was supported by grant NMRC/CBRG/0073/2014. The Y. M. laboratory was supported by the grant of MOE Tier 1 RG146/17 from Ministry of Education Singapore.

Declaration of Competing Interest

The authors declare no conflicts of interest related to any work reported here.

Appendix A. Supplementary data

Supplementary data to this article can be found online at https://doi.org/10.1016/j.jmb.2019.07.033.

Received 1 May 2019;
Received in revised form 25 July 2019;
Accepted 27 July 2019
Available online 2 August 2019

Keywords:
allosteric regulation;
structural dynamics;
metabolic reprogramming;
stress response

W.Z., J.G. and L.C. contributed equally to this work.

‡Present addresses: Y.H. Chionh, Tychan Private Ltd., 80 Robinson Road, #17-02, Singapore 068898, Singapore.

Abbreviations used:
CCM, central carbon metabolism; F6P, fructose 6-phosphate; G3P, glyceraldehyde 3-phosphate; G6P, glucose 6-phosphate; *Mtb*PYK, *Mycobacterium tuberculosis* pyruvate kinase; OX, oxalate; PEP, phosphoenolpyruvate; R5P, ribose 5-phosphate; X5P, xylulose 5-phosphate; 5RP, ribulose 5-phosphate.

References

[1] D. Brites, S. Gagneux, Co-evolution of *Mycobacterium tuberculosis* and Homo sapiens, Immunol. Rev. 264 (2015) 6–24, https://doi.org/10.1111/imr.12264.
[2] S. Gagneux, Host–pathogen coevolution in human tuberculosis, Philos. Trans. R. Soc. Lond. Ser. B Biol. Sci. 367 (2012) 850–859.
[3] C. Nathan, Taming tuberculosis: a challenge for science and society, Cell Host Microbe 5 (2009) 220–224.
[4] Transcriptional adaptation of *Mycobacterium tuberculosis* within macrophages: insights into the phagosomal environment, J. Exp. Med. 198 (2003) 693–704.
[5] L.P.S. de Carvalho, S.M. Fischer, J. Marrero, C. Nathan, S. Ehrt, K.Y. Rhee, Metabolomics of *Mycobacterium tuberculosis* reveals compartmentalized co-catabolism of carbon substrates, Chem. Biol. 17 (2010) 1122–1131.
[6] T. Noy, O. Vergnolle, T.E. Hartman, K.Y. Rhee, W.R. Jacobs, M. Berney, et al., Central role of pyruvate kinase in carbon co-catabolism of *Mycobacterium tuberculosis*, J. Biol. Chem. 291 (2016) 7060–7069.
[7] B.M. Cumming, A.J.C. Steyn, Metabolic plasticity of central carbon metabolism protects mycobacteria, Proc. Natl. Acad. Sci. U. S. A. 112 (2015) 13135–13136.
[8] T. Wagner, M. Bellinzoni, A. Wehenkel, H.M. O'Hare, P.M. Alzari, Functional plasticity and allosteric regulation of α-ketoglutarate decarboxylase in central mycobacterial metabolism, Chem. Biol. 18 (2011) 1011–1020.
[9] H. Eoh, E. Layre, R. Morris, D.B. Moody, K.Y. Rhee, Metabolic anticipation in *Mycobacterium tuberculosis*, Nat. Microbiol. 2 (2017), 17084.
[10] S. Ehrt, D. Schnappinger, K.Y. Rhee, Metabolic principles of persistence and pathogenicity in *Mycobacterium tuberculosis*, Nat. Rev. Microbiol. 16 (2018) 496–507.
[11] Y.H. Chionh, M. McBee, I.R. Babu, F. Hia, W. Lin, W. Zhao, et al., tRNA-mediated codon-biased translation in mycobacterial hypoxic persistence, Nat. Commun. 1 (2016), 13302.
[12] W. Zhong, L. Cui, Q. Cai, P. Ho, M. Yuan, A.E. Sahili, et al., Allosteric pyruvate kinase-based "logic gate" synergistically senses energy and sugar levels in *Mycobacterium tuberculosis*, Nat. Commun. 8 (2017) 693.
[13] M. Yuan, I.W. McNae, Y. Chen, E.A. Blackburn, M.A. Wear, P.A.M. Michels, et al., An allostatic mechanism for M2 pyruvate kinase as an amino-acid sensor, Biochem. J. 475 (2018) 1821–1837.
[14] D. Anastasiou, G. Poulogiannis, J.M. Asara, M.B. Boxer, J.-K. Jiang, M. Shen, et al., Inhibition of pyruvate kinase M2 by reactive oxygen species contributes to cellular antioxidant responses, Science. 334 (2011) 1278–1283.
[15] W. Zhong, H.P. Morgan, I.W. McNae, P.A.M. Michels, L.A. Fothergill-Gilmore, M.D. Walkinshaw, `in crystallo' substrate binding triggers major domain movements and reveals magnesium as a co-activator of *Trypanosoma brucei*

pyruvate kinase, Acta Crystallogr. D Biol. Crystallogr. 69 (2013) 1768–1779.
[16] H.P. Morgan, I.W. McNae, M.W. Nowicki, V. Hannaert, P.A. M. Michels, L.A. Fothergill-Gilmore, et al., Allosteric mechanism of pyruvate kinase from *Leishmania mexicana* uses a rock and lock model, J. Biol. Chem. 285 (2010) 12892–12898.
[17] H.P. Morgan, W. Zhong, I.W. McNae, P.A.M. Michels, L.A. Fothergill-Gilmore, M.D. Walkinshaw, Structures of pyruvate kinases display evolutionarily divergent allosteric strategies, Royal Soc. Open Sci. 1 (2014) 140120.
[18] Z. Yuan, J. Zhao, Z.-X. Wang, Flexibility analysis of enzyme active sites by crystallographic temperature factors, Protein Eng. 16 (2003) 109–114.
[19] J. Guo, H.-X. Zhou, Allosteric activation of SENP1 by SUMO1 β-grasp domain involves a dock-and-coalesce mechanism, Elife. 5 (2016) 722.
[20] J. Guo, X. Pang, H.-X. Zhou, Two pathways mediate interdomain allosteric regulation in pin1, Structure. 23 (2015) 237–247.
[21] G. Stetz, G.M. Verkhivker, Probing allosteric inhibition mechanisms of the Hsp70 chaperone proteins using molecular dynamics simulations and analysis of the residue interaction networks, J. Chem. Infor. Mod. 56 (2016) 1490–1517.
[22] C. Boon, T. Dick, *Mycobacterium bovis* BCG response regulator essential for hypoxic dormancy, J. Bacteriol. 184 (2002) 6760–6767.
[23] K.L. Low, P.S.S. Rao, G. Shui, A.K. Bendt, K. Pethe, T. Dick, et al., Triacylglycerol utilization is required for regrowth of in vitro hypoxic nonreplicating *Mycobacterium bovis* bacillus Calmette–Guerin, J. Bacteriol. 191 (2009) 5037–5043.
[24] S. Ahn, J. Jung, I.-A. Jang, E.L. Madsen, W. Park, Role of glyoxylate shunt in oxidative stress response, J. Biol. Chem. 291 (2016) 11928–11938.
[25] S.R. Maloy, M. Bohlander, W.D. Nunn, Elevated levels of glyoxylate shunt enzymes in *Escherichia coli* strains constitutive for fatty acid degradation, J. Bacteriol. 143 (1980) 720–725.
[26] H.L. Kornberg, The role and control of the glyoxylate cycle in *Escherichia coli*, Biochem. J. 99 (1966) 1–11.
[27] J. Schaub, C. Schiesling, M. Reuss, M. Dauner, Integrated sampling procedure for metabolome analysis, Biotechnol. Prog. 22 (2006) 1434–1442.
[28] B.D. Bennett, E.H. Kimball, M. Gao, R. Osterhout, S.J. Van Dien, J.D. Rabinowitz, Absolute metabolite concentrations and implied enzyme active site occupancy in *Escherichia coli*, Nat. Chem. Biol. 5 (2009) 593–599.
[29] R. Zoraghi, R.H. See, H. Gong, T. Lian, R. Swayze, B.B. Finlay, et al., Functional analysis, overexpression, and kinetic characterization of pyruvate kinase from methicillin-resistant *Staphylococcus aureus*, Biochem. 49 (2010) 7733–7747.
[30] R. Kapoor, T.A. Venkitasubramanian, Glucose 6-phosphate activation of pyruvate kinase from *Mycobacterium smegmatis*, Biochem. J. 193 (1981) 435–440.
[31] G. Prakasam, M.A. Iqbal, R.N.K. Bamezai, S. Mazurek, Posttranslational modifications of pyruvate kinase M2: tweaks that benefit cancer, Front. Oncol. 8 (2018) 309.
[32] A. Kumar, A. Farhana, L. Guidry, V. Saini, M. Hondalus, A.J. C. Steyn, Redox homeostasis in mycobacteria: the key to tuberculosis control? Expert Rev. Mol. Med. 13 (2011) e39.
[33] I. Pecsi, K. Hards, N. Ekanayaka, M. Berney, T. Hartman, W. R. Jacobs, et al., Essentiality of succinate dehydrogenase in *Mycobacterium smegmatis* and its role in the generation of the membrane potential under hypoxia, MBio. 5 (2014), 81318.
[34] J.A. Imlay, The molecular mechanisms and physiological consequences of oxidative stress: lessons from a model bacterium, Nat. Rev. Microbiol. 11 (2013) 443–454.
[35] A. Kumar, J.C. Toledo, R.P. Patel, J.R. Lancaster, A.J.C. Steyn, *Mycobacterium tuberculosis* DosS is a redox sensor and DosT is a hypoxia sensor, Proc. Natl. Acad. Sci. U. S. A. 104 (2007) 11568–11573.
[36] S.K. Spaans, R.A. Weusthuis, J. van der Oost, S.W.M. Kengen, NADPH-generating systems in bacteria and archaea, Front. Microbiol. 6 (2015) 742.
[37] T.G.G. Battye, L. Kontogiannis, O. Johnson, H.R. Powell, A. G.W. Leslie, iMOSFLM: a new graphical interface for diffraction-image processing with MOSFLM, Acta Crystallogr. D Biol. Crystallogr. 67 (2011) 271–281.
[38] P. Evans, IUCr, scaling and assessment of data quality, Acta Crystallogr. D Biol. Crystallogr. 62 (2006) 72–82.
[39] P.R. Evans, G.N. Murshudov, IUCr, how good are my data and what is the resolution? Acta Crystallogr. D Biol. Crystallogr. 69 (2013) 1204–1214.
[40] A.J. McCoy, R.W. Grosse-Kunstleve, P.D. Adams, M.D. Winn, L.C. Storoni, R.J. Read, Phaser crystallographic software, J. Appl. Crystallogr. 40 (2007) 658–674.
[41] P. Emsley, K. Cowtan, Coot: model-building tools for molecular graphics, Acta Crystallogr. D Biol. Crystallogr. 60 (2004) 2126–2132.
[42] G.N. Murshudov, P. Skubák, A.A. Lebedev, N.S. Pannu, R.A. Steiner, R.A. Nicholls, et al., REFMAC5 for the refinement of macromolecular crystal structures, Acta Crystallogr. D Biol. Crystallogr. 67 (2011) 355–367.
[43] I.W. Davis, A. Leaver-Fay, V.B. Chen, J.N. Block, G.J. Kapral, X. Wang, et al., MolProbity: all-atom contacts and structure validation for proteins and nucleic acids, Nucleic Acids Res. 35 (2007) W375–W383.
[44] W.L. DeLano, The PyMOL Molecular Graphics System [Computer Program], DeLano Scientific, San Carlos, CA, USA, 2002.
[45] D.A. Case, T.E. Cheatham, T. Darden, H. Gohlke, R. Luo, K. M. Merz, et al., The Amber biomolecular simulation programs, J. Comput. Chem. 26 (2005) 1668–1688.
[46] J.-P. Ryckaert, G. Ciccotti, H.J.C. Berendsen, Numerical integration of the cartesian equations of motion of a system with constraints: molecular dynamics of n-alkanes, J. Comput. Phys. 23 (1977) 327–341.
[47] U. Essmann, L. Perera, M.L. Berkowitz, T. Darden, H. Lee, L. G. Pedersen, A smooth particle mesh Ewald method, J. Chem. Phys. 103 (1995) 8577–8593.
[48] D.R. Roe, T.E. Cheatham, PTRAJ and CPPTRAJ: software for processing and analysis of molecular dynamics trajectory data, J. Chem. Theory Comput. 9 (2013) 3084–3095.
[49] L.G. Wayne, L.G. Hayes, An in vitro model for sequential study of shiftdown of *Mycobacterium tuberculosis* through two stages of nonreplicating persistence, Infect. Immun. 64 (1996) 2062–2069.
[50] Essential roles of methionine and S-adenosylmethionine in the autarkic lifestyle of *Mycobacterium tuberculosis*, Proc. Natl. Acad. Sci. U. S. A. 112 (2015) 10008–10013.
[51] L. Cui, Y.H. Lee, T.L. Thein, J. Fang, J. Pang, Y.S. Leo, et al., Serum metabolomics reveals serotonin as a predictor of severe dengue in the early phase of dengue fever, PLoS Negl. Trop. Dis 10 (2016) e0004607.